Three-dimensional MHD Magnetic Reconnection Simulations with Finite Guide Field: Proposal of the Shock-Evoking Positive-Feedback Model

Shuoyang Wang and Takaaki Yokoyama

Department of Earth and Planetary Science, The University of Tokyo, 7-3-1 Hongo,

Bunkyo-ku, Tokyo, 113-0033, Japan

wangshuoyang@eps.s.u-tokyo.ac.jp

and

Hiroaki Isobe

Shishukan, Kyoto University, Yoshidanakaadachicho, Kyoto Sakyo-ku, Kyoto 606-8306,

Japan

Received

accepted _____

Not to appear in Nonlearned J., 45.

ABSTRACT

Using a three-dimensional magnetohydrodynamic model, we simulate the magnetic reconnection in a single current sheet. We assume a finite guide field, a random perturbation on the velocity field and uniform resistivity.

Our model enhances the reconnection rate relative to the classical Sweet-Parker model in the same configuration. The efficiency of magnetic energy conversion is increased by interactions between the multiple tearing layers coexisting in the global current sheet. This interaction, which forms a positive-feedback system, arises from coupling of the inflow and outflow regions in different layers across the current sheet. The coupling accelerates the elementary reconnection events, thereby enhancing the global reconnection rate. The reconnection establishes flux tubes along each tearing layer. Slow-mode shocks gradually form along the outer boundaries of these tubes, further accelerating the magnetic energy conversion. Such positive-feedback system is absent in two-dimensional simulation, three-dimensional reconnection without a guide field and a reconnection under a single perturbation mode. We refer to our model as the "shock-evoking positivefeedback" model.

Subject headings: (magnetohydrodynamics:) MHD, plasmas, magnetic reconnection, - methods:numerical

1. Introduction

Magnetic reconnection is considered to source the rapid conversion of magnetic energy in various solar coronal activities with extremely high Lundquist number $S = Lv_A/\tilde{\eta} \sim 10^{14}$, where L, v_A and $\tilde{\eta}$ denote the current sheet length, Alfvén speed and magnetic diffusivity, respectively. The two classical reconnection models are the Sweet-Parker model (Sweet 1958; Parker 1963) and Petschek's model (Petschek 1964). In the Sweet-Parker model, the reconnection rate scales as $v_{inflow}/v_A \sim 1/\sqrt{S}$, several orders of magnitude slower than required in many solar and astronomical applications. The Petschek's model yields a sufficiently fast reconnection rate ($\sim 1/\ln S$) by virtue of the localized diffusion region and the extended slow-mode shocks. The localized diffusion region is thought to originate from microscopic plasma processes occurring on scales many orders of magnitude smaller than the global scale. Thus, it is necessary to address the huge scale gap between the micro and the global scales while maintaining efficient global energy conversion.

Biskamp (1986) argued that Sweet-Parker sheets with aspect ratio (i.e., length to thickness) exceeding 100 are vulnerable to secondary tearing instability. Shibata and Tanuma (2001) developed a fractal reconnection model based on this concept. They reasoned that once plasmoids are formed by the primary tearing instability, plasmoid ejection and growth stretch the intervening current sheets, increasing the aspect ratio of the current sheets. Eventually these current sheets become unstable to secondary tearing, and disintegrate into chains of smaller-scale plasmoids and current sheets. By this stepwise process, an initially long and thick current sheet can reduce to the scale of the ion Larmor radius or ion inertial length. This hierarchical structure can plausibly couple the largest and smallest scales. High-resolution numerical simulations have proved the feasibility of this scheme (Bárta et al. 2011) and also showed that the reconnection rate becomes independent of the Lundquist number when $S \gtrsim S_c \sim 10^4$ (e.g., Loureiro et al. 2012). This fractal reconnection model assumes translational invariance in the direction perpendicular to the reconnection plane. This assumption is violated in the presence of three-dimensional (3D) instabilities, such as the kink-like instability reported by Dahlburg et al. (1992). These authors found fast growth and saturation of the tearing mode along the anti-parallel magnetic field. Meanwhile, the oblique modes (with a component perpendicular to the tearing plane) continue growing and dominate in the later phase. Moreover, in the absence of a guide field, this kink-like instability will suppress the coalescence instability in the tearing layer, completely breaking the initial laminar structure (Dahlburg and Einaudi 2002). This instability is expected to affect the fractal reconnection in 3D scenario.

Another concern is the emergence of multiple tearing layers (Galeev and Zelenyi 1977). When a sheared current sheet is subjected to a multi-modal perturbation (comprising modes) $\mathbf{k_1},\mathbf{k_2},...,\mathbf{k_n}),$ multiple layers whose local magnetic field orientation satisfy $\mathbf{k}\cdot\mathbf{B}=0$ can emerge and are expected to interact when they become sufficiently close. Interaction should disrupt the laminar structures of the layers, altering their internal fractal reconnections. Onofri et al. (2004) studied the nonlinear evolution of several tearing layers coexisting inside a sheared current sheet in an incompressible plasma. They found that although the two-dimensional (2D) mode grows more rapidly than the emerging modes in a linear analysis, the emerging modes are oblique modes at an early stage. The resulting energy cascade gradually extends outwards from the current sheet center, leading to a final turbulent state. Moreover, the inverse energy transfer implies coalescence of the magnetic islands. Landi et al. (2008) further confirmed the three-dimensionality of the initially emerging modes in a compressible plasma simulation. Thus, the preferred source of plasmoid instability growth is changed and the reconnection enhancement concept should be modified in the 3D case. But neither Onofri et al. (2004) nor Landi et al. (2008) explicitly discussed the changes in the reconnection rate. For this purpose, we seek more details of

the magnetic energy consumption.

This paper presents a detailed study of magnetic reconnection under tearing instability in a 3D resistive compressive MHD environment with a finite guide field. In Section 2, we introduce the simulation model. In Section 3 and 4, simulation result and its discussion are presented. Section 5 makes a summary of the whole study.

2. Simulation Model

The 3D resistive MHD equations are solved in Cartesian coordinates. Viscosity, gravity and heat conduction are neglected for simplicity. The basic equations are as follows:

$$\frac{\partial \rho}{\partial t} + (\mathbf{v} \cdot \nabla)\rho = -\rho(\nabla \cdot \mathbf{v}) \tag{1}$$

$$\rho\left(\frac{\partial \mathbf{v}}{\partial t} + (\mathbf{v} \cdot \nabla)\mathbf{v}\right) = -\nabla p + \frac{\mathbf{J} \times \mathbf{B}}{c}$$
(2)

$$\mathbf{J} = \frac{c}{4\pi} \nabla \times \mathbf{B} \tag{3}$$

$$\frac{\partial p}{\partial t} + (\mathbf{v} \cdot \nabla)p = -\gamma p(\nabla \cdot \mathbf{v}) + (\gamma - 1)\eta \mathbf{J}^2$$
(4)

$$\frac{\partial \mathbf{B}}{\partial t} = \nabla \times (\mathbf{v} \times \mathbf{B} - c\eta \mathbf{J}) \tag{5}$$

$$p = \frac{\rho}{\bar{m}} k_B T. \tag{6}$$

Here, k_B is the Boltzmann constant, η is the resistivity, $\gamma = 5/3$, c is the speed of light, and \bar{m} is the mean particle mass. For a fully ionized hydrogen gas, $\bar{m} = 0.5m_p$, where m_p is the proton mass. The other variables take their usual meanings.

All quantities are normalized by their characteristic values. The length scale is the width of the initial current sheet (= δ). The time scale is normalized by $t_A = \delta/v_{A0}$, where v_{A0} is the Alfvén velocity. The initial mass density ρ_0 normalizes the mass density.

The magnetic field is normalized by $B_0 = v_{A0}\sqrt{\rho_0}$. Consequently, the current density is normalized by $J_0 = cB_0/\delta$ and the plasma pressure is normalized by $p_0 = B_0^2$.

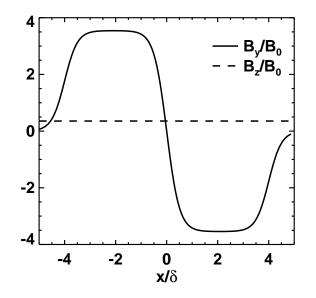


Fig. 1.— Initial magnetic field plot along y = 0, z = 0. Solid line is the normalized $B_y(x, y = 0, z = 0)$ and dashed line is the normalized $B_z(x, y = 0, z = 0)$.

The initial magnetic field comprises an anti-parallel component $B_y(x)$ and a uniform finite guide field B_z , as plotted in Fig. 1:

$$\mathbf{B} = B_y \mathbf{e}_y + B_z \mathbf{e}_z$$
$$= B_{y0} \tanh\left(\frac{x}{0.5\delta}\right) \left\{ \frac{1}{2} \left[\tanh\left(\frac{|x| - 4\delta}{0.5\delta}\right) - 1 \right] \right\} \mathbf{e}_y + \alpha B_{y0} \mathbf{e}_z \tag{7}$$

where $B_{y0} = \sqrt{4\pi}B_0$ and α controls the magnitude of the guide field B_z . Here we adopt $\alpha = 0.1$ in the basic model. A magnetic field with non-zero α shears the structure along the *x*-axis. The magnetic diffusivity is assumed to be spatially and temporally constant with a magnitude of $\tilde{\eta} = c^2 \eta / (4\pi) \sim 3 \times 10^{-4} \delta^2 / t_A$. Resulting Lundquist number is thus defined by the Alfvén speed $v_A = v_{A0}\sqrt{1 + \alpha^2}$, $S = v_A L_y / (2\tilde{\eta}) \sim 2.6 \times 10^5$.

The simulation begins with a uniform mass density ρ_0 throughout the simulation space.

Pressure balance between the gas and magnetic field is also maintained in the whole box, giving:

$$p + \frac{B^2}{8\pi} = \frac{B_0^2}{2} (1 + \alpha^2)(1 + \beta)$$
(8)

in which β is the ratio between the plasma and magnetic field pressures at the minimum plasma pressure; we set $\beta = 0.2$.

To initiate the reconnection, we add a random velocity perturbation with small amplitude $(v_x, v_y, v_z \leq 1 \times 10^{-3} v_{A0})$ over the whole simulation domain. Short-wavelength perturbations are eliminated. The remaining waves satisfy $1/k_y^2 + 1/k_z^2 \geq 116\delta^2$, also limited by $|k_y\delta| \leq 2$ and $|k_z\delta| \leq 2$.

The simulation box size $(L_x \times L_y \times L_z)$ is $10\delta \times 24\delta \times 6\delta$, containing $240 \times 768 \times 192$ grids. To resolve the tearing layer, we construct non-uniform grids with $\Delta x \ge 0.02\delta$ along the *x*-direction. Uniform grids with $\Delta y = \Delta z = 0.03125\delta$ are constructed in the *y*- and *z*-directions. Periodic boundary conditions are imposed on each border. The calculations are performed in CIP-MOCCT code (Kudoh et al. 1999) with an artificial Lapidus viscosity (Lapidus 1967).

3. Simulation results

The efficiency of the magnetic energy conversion is approximately five times higher in our 3D reconnection than in the Sweet-Parker reconnection. We propose a detailed mechanism of reconnection enhancement, referring to our new model as the "shock-evoking positive-feedback" model.

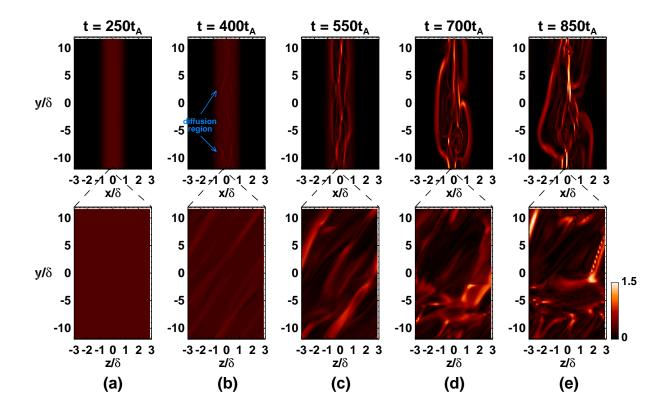


Fig. 2.— Current density $|\mathbf{J}|/J_0$ in the z = 0 plane (upper panel) and in the $x = -0.3\delta$ plane (lower panel).

3.1. Global structure

The upper and lower panels of Fig. 2 show the temporal evolution of the current density $|\mathbf{J}|/J_0$ in the xy-plane (z = 0) and the zy-plane $(x = -0.3\delta)$, respectively. In the early phase (Fig. 2(a)), diffusion dominates and no clear pattern is observed inside the primary (central) current sheet. Gradually, tearing instability (Furth et al. 1963) emerges and two chains of smaller diffusion regions (or reconnection sites) develop and grow adjacent to $x = \pm 0.3\delta$ (Fig. 2(b)). Within these chains, the current density is much higher than the surroundings. The chains form a web-like pattern across the global current sheet. Fig. 3 and Fig. 4 present the plasma density, pressure, velocity, magnetic field, and current density at $t = 400t_A$ and $700t_A$ respectively, in the z = 0 plane. The Δ notation defines a difference;

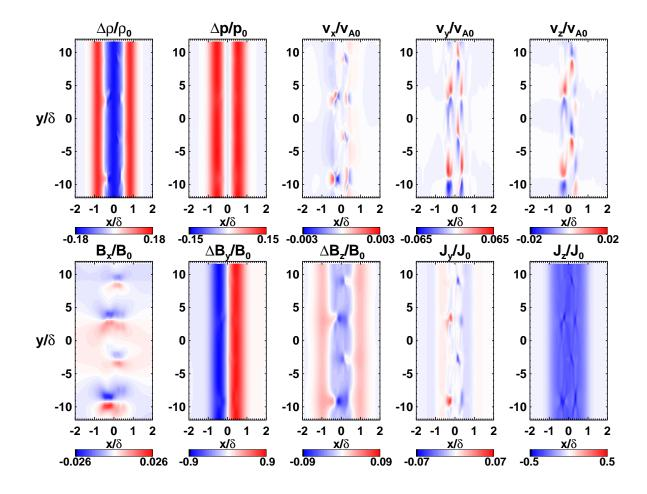


Fig. 3.— Global patterns of variables on the z = 0 plane at $t = 400t_A$; plasma density difference $(\Delta \rho)$, pressure difference (Δp) , velocity components (v_x, v_y, v_z) , magnetic field components (B_x) and differences $(\Delta B_y, \Delta B_z)$, current density component (J_y, J_z)

for example, $\Delta \rho$ is defined as $\Delta \rho = \rho - \rho_{initial}$, where $\rho_{initial}$ is the initial value of ρ . The structures are well-organized in each plot of Fig. 3, but becomes distorted by flows in the later phase (Fig. 4).

Oblique lines (diffusion lines) are formed by the diffusion regions in the zy-plane, as shown in the lower panel of Fig. 2(b). The positions of these diffusion lines along the x-axis are determined by resonance layers (resonant tearing layers), which arise from the periodic boundary conditions in the y- and z- directions. This slab structure resembles

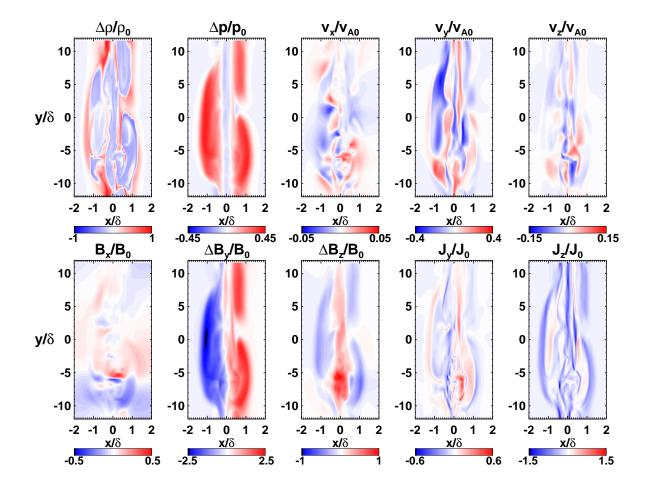


Fig. 4.— Global patterns on the z = 0 plane at $t = 700t_A$. Variables are defined in the same way as Fig. 3.

the cylindrically symmetric rational surface in a tokamak (e.g., Bellan 2006). The safety factor q, which denotes the period of the magnetic field lines cycling (sheet-wise) across the zy-plane, is calculated along the x-axis as follows:

$$q(x) = \frac{L_y}{L_z} \left| \frac{\langle B_z \rangle_x}{\langle B_y \rangle_x} \right|.$$
(9)

Here, L_y and L_z are the box sizes in the y- and z-directions, respectively. $\langle B_y \rangle_x$ and $\langle B_z \rangle_x$ are the mean magnetic field components on the zy-plane at the corresponding point x. Strictly speaking, provided that the q value in a zy-plane satisfies

$$q = \frac{m}{n} \tag{10}$$

where m and n are integers, the wave signal is strengthened and the layer develops into a resonance layer. Clearly numerous layers are expected. However, due to the different growth rates of these modes, a limited number of layers can resonate locally. When m and nare large, the corresponding wavelength is small; hence, the instability is easily suppressed by magnetic tension force.

The safety factors calculated by Eq. (9) at $t = 250t_A$ are plotted as black solid line in the upper panel of Fig. 5. To find the most unstable mode in the box, the Fourier transformation of the current density $|\mathbf{J}|/J_0$ on each zy-plane is calculated along the x-axis. The signal intensity is calculated as

$$f_i(x,k_z,k_y) = \left| \int_{-\frac{L_z}{2}}^{\frac{L_z}{2}} \int_{-\frac{L_y}{2}}^{\frac{L_y}{2}} [|\mathbf{J}(x,y,z)|/J_0] e^{-i2\pi(k_z z + k_y y)} dy dz \right|^2.$$
(11)

Here, k_y and k_z are wavenumbers (defined as $k = 1/\lambda$, where λ is the wavelength) in the y- and z-directions, respectively. The intensity increases and fades when approaching and departing a resonance layer, respectively. The changes in f_i and $|\mathbf{J}|/J_0$ along the x-axis are demonstrated in five slices at $x = -0.5\delta$, -0.3δ , $0, 0.3\delta$, 0.5δ (see middle and lower panels of Fig. 5). The black dash-dotted lines in the middle panels indicate the vectors perpendicular to the local magnetic field. On certain resonance layer ($x = \pm 0.3\delta$), the line coincides with the maximum signal since it must satisfy $\mathbf{k} \cdot \mathbf{B} = 0$, where $\mathbf{k} = k_y \mathbf{e_y} + k_z \mathbf{e_z}$. As B_y changes sign across x = 0, the dominant \mathbf{k} in the resonance layers reverses the sign of one of its component while preserving another. The blue solid line in the upper panel of Fig. 5 plots the maximum of f_i on each zy-plane along x-direction, $\max_{k_z,k_y}(f_i)$, as a function of x. We find that $\max_{k_z,k_y}(f_i)$ peaks several times inside the primary current sheet. Comparisons with the q curve reveal that these peaks correspond to resonance layers with q = 1 and

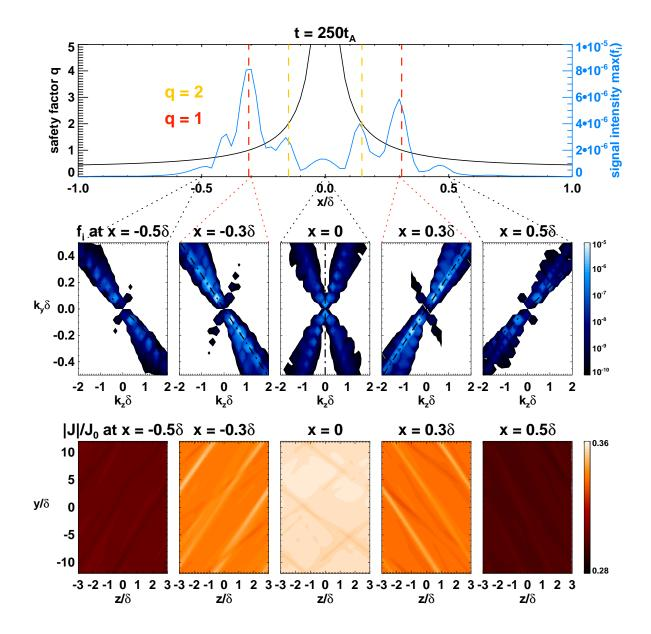


Fig. 5.— Upper panel: safety factor q and local maximum $\max_{k_z,k_y}(f_i)$ at points along the x-axis. Middle panel: f_i in k-space in selected zy-planes. Lower panel: normalized $|\mathbf{J}|$ in the corresponding layers.

q = 2 (red and orange dashed lines respectively in upper panel of Fig. 5). Resonance layers with other q values are missing in this model, possibly because that the large-q resonance

layers near the center (x = 0) are separated by less than the spatial resolution of the simulation. It is also likely that the most unstable tearing mode in this configuration is the 3D mode $(k_z \neq 0)$ rather than a 2D mode $(k_z = 0)$, and the modes on layers with $q \ge 3$ grow at smaller rates than the modes on layers with q = 1 and q = 2 (Baalrud et al. 2012).

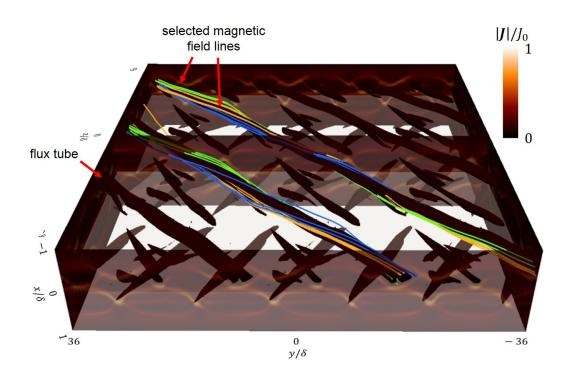


Fig. 6.— Coherent structure of flux tubes extracted from the isosurfaces of current density $|\mathbf{J}|/J_0 = 0.12$ at $t = 500t_A$. The plotting area in the *y*- and *z*-directions is expanded by a factor of 3. Translucent white surface represents the x = 0 plane. Colored solid lines are selected magnetic field lines.

As the guide field is uniform, no null points or sheets exist. The magnetic field lines reconnect across the tearing layers and only part of the field strength is consumed. These component reconnections lead to twisting reconnected field lines that cross the resonance layer to and fro in 3D space. The field lines form coherent flux tubes whose width along the *zy*-plane approximately equals the wavelength λ of the tearing mode ($\lambda = 2.9\delta$ and 5.4δ on q = 1 and q = 2 planes, respectively). The flux tube structure can be extracted from the isosurfaces of the current density, as shown in Fig. 6 (since periodic boundary conditions are assumed, the plotting area in the y- and z-directions is extended by a factor of 3). Twisting field lines wind around the flux tubes. The tilting angle of the flux tubes reverses across the x = 0 plane (indicated by the translucent white surface in Fig. 6).

Later, as the local reconnection events gradually develop in the individual diffusion regions, the flux tubes thicken along the x-direction. The outflows from the diffusion regions are sufficiently accelerated to distort the well-organized structure (Fig. 2(c)). The flux tubes centered at the negative-x side collide and coalesce (Fig. 2(d)). Finally, only spatially extended current sheets and large flux tubes remain (Fig. 2(e)).

Actually there are three current sheets coexisting inside the whole simulation box. It could be seen clearly that the current sheets at the boundary have no significant influence on the current sheet at the center (Fig. 7). Furthermore, We test a reconnection model with twice the length along x-direction to see the effect of the boundary and the result does not change.

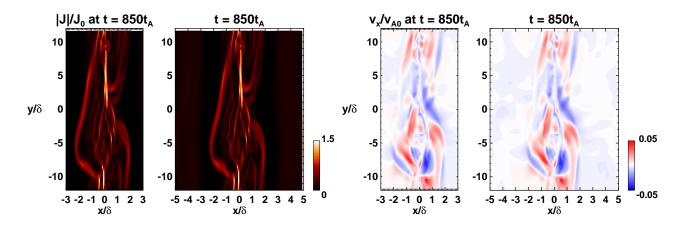


Fig. 7.— Current density $|\mathbf{J}|/J_0$ and velocity v_x/v_{A0} in the z = 0 plane by comparing plot ranges from -3δ to 3δ and plot ranges from -5δ to 5δ .

3.2. Reconnection rate

To understand the reconnection efficiency, we acquire the reconnection rate calculated as follows:

$$M_A = \left| \frac{d}{dt} \int \epsilon_m dV \right| \left/ \left(2L_y L_z \frac{B_{y0}^2}{4\pi} v_{A0} \right).$$
(12)

In the numerator of Eq. (12), the magnetic energy density ϵ_m is integrated over the volume inside the primary global current sheet to obtain the total magnetic energy. The boundary of the primary current sheet is determined from the specified critical plasma pressure $p_c \sim 0.008B_0^2$. The energy inside the considered sheet is conserved by adding the surface flux term along the x-direction in Eq. (4). The result is plotted in Fig. 8. The reconnection rate is rapidly enhanced after $t = 450t_A$.

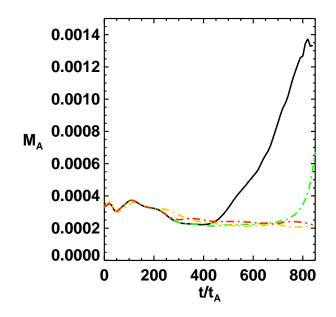


Fig. 8.— Reconnection rate in the basic model (black solid line), whose maximum is about 5 times of the Sweet-Parker type reconnection simulated in the same 3D box (not plotted).
2.5D simulation with the guide field (green dash-dotted line), 3D simulation without a guide field (orange dash-dotted line), and 3D simulation with a single mode (red dash-dotted line).

To check whether 3D reconnection is sufficiently fast, we simulated the Sweet-Parker type reconnection in the same 3D box. This model begins with four large vortices imitating the inflow-outflow coupling in a single reconnection. The velocity components are constrained by $v_x, v_y \leq 2 \times 10^{-4} v_{A0}$ and $v_z = 0$. Translational invariance is maintained at the beginning. The Sweet-Parker reconnection rate, which is not plotted in Fig. 8, is 0.00026, which is approximately 1/5 the reconnection rate of the basic model.

To better quantify the effect of the third dimension on the reconnection, we conduct a 2.5D simulation with a guide field (green dash-dotted line in Fig. 8). The initial velocity field is the initial velocity field on the z = 0 plane in the basic model. Because $k_z = 0$ (or $L_z \to \infty$) throughout the simulation box, the resonance layer is limited in x = 0 plane. A secondary instability (plasmoid instability) starts to develop at the end of this simulation, and the reconnection rate increases later than in the basic model. In comparison, no finer filamentary structures are detected in the basic model. Then the reconnection rate increase in the basic model is due to a secondary instability other than plasmoid instability.

To generate oblique tearing layers, we also require a finite guide field. If the initial magnetic field has no z-component ($\alpha = 0$), the tearing mode can grow only along the x = 0 plane, across which the magnetic field reverses. The result of a 3D simulation without the guide field is plotted as the orange dash-dotted line in Fig. 8. In this model, the initial velocity is randomly perturbed as in the basic model. Clearly, the reconnection is much lower in this simulation than in the basic model.

As shown in the previous result, the basic model admits several tearing layers coexisting in the same current sheet. To understand the importance of these multiple layers, we conduct a 3D simulation with a single mode (\mathbf{k}) in the perturbed velocity field (red dash-dotted line in Fig. 8). The selected \mathbf{k} is the most unstable mode in the leftmost resonance layer (at the negative x-side) of the basic model. The reconnection rate in this

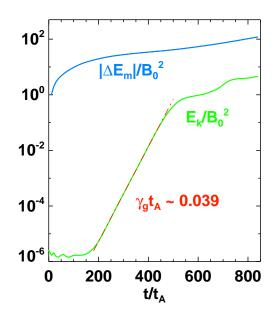


Fig. 9.— Development of total consumed magnetic energy (blue solid line) and total kinetic energy (green solid line). Red dash-dotted line represents exponential growth.

model is $\sim 20\%$ that of the basic model throughout the same development period. The reconnection within each diffusion region gradually saturates rather than largely increases. This result confirms that the reconnection rate is enhanced by multiple resonance layers coexisting in one current sheet.

To quantitatively examine the energy conversion efficiency, we plot the temporal evolutions of the normalized total kinetic energy E_k/B_0^2 , and the consumed total magnetic energy $|\Delta E_m|/B_0^2$ of the central global current sheet in Fig. 9. The kinetic energy grows exponentially from $t = 200t_A$ to $t = 450t_A$. From exponential fitting, we find that $\gamma_g t_A \sim 0.039$, where $\gamma_g = d(\ln E_k)/dt$. Comparing these results with the reconnection rate, it is easily seen that rapid enhancement immediately follows the exponential growth of kinetic energy (at $t = 450t_A$). Moreover, the tearing layers are already recognizable around this time (see Fig. 2(b)). Together with the above findings, this implies that the interaction between fully grown tearing layers triggers the fast consumption of magnetic energy. Regarding the different reconnection rates plotted in Fig. 8, we conclude that the interaction between different resonance layers is crucial for the enhanced reconnection in later phase.

3.3. Positive-feedback system

On closer examination, the diffusion regions on multiple tearing layers are observed to form a web-like pattern across the current sheet. Fig. 10 plots the current density $|\mathbf{J}|/J_0$ on the z = 0 plane at various times of the simulation $(t = 450t_A, t = 500t_A, and$ $t = 550t_A$), overlaid with the velocity flows (white arrows) and the z-component of the vorticity ω_z/ω_0 , where $\omega_0 = v_{A0}/\delta$. On this plane, the small diffusion regions form an asymmetric structure with a zigzag pattern. Within this structure, the diffusion regions on different resonance layers are apart with each other in y-direction. Examining the local stream, we find that the outflow from one reconnection site diverts and feeds into the inflow region of the reconnection site on a different resonance layer. Meanwhile, a portion of the reconnected magnetic flux is transported, where it can again participate in reconnection. The transportation is regulated by the outflow from the diffusion region. The outflow strengthens as the local reconnection proceeds, implying that faster flux transportation correspondingly enhances the inflow, thus accelerating the local reconnection. This coupling, named as positive-feedback system, is generated by the existence of multiple tearing layers, in contrast to the self-feeding system inside a current sheet with a single reconnection layer reported by Lapenta (2008). The coupling of inflow and outflow regions across the current sheet can be identified by the coalescence of branch-like structures, which extend from the individual diffusion regions in the contour plots of ω_z . An example of such coupling is delineated by the black dashed rectangle in the lower panels of Fig. 10. Although this feature is gradually deformed by the turbulence developing inside the current sheet, the

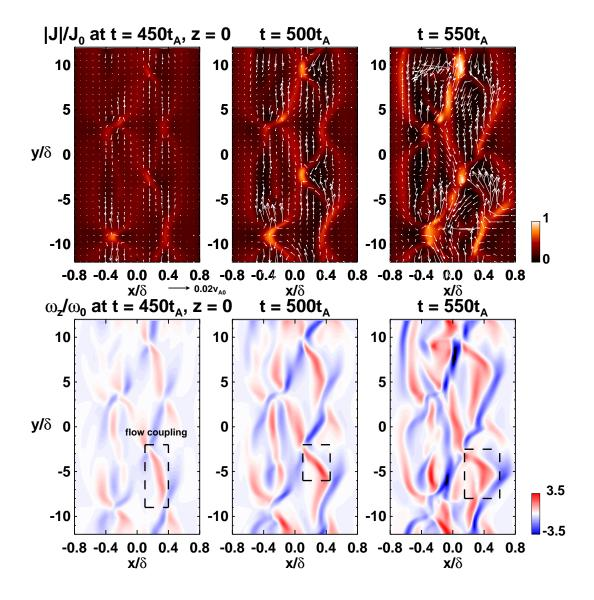


Fig. 10.— Snapshots of current density $|\mathbf{J}|/J_0$ and the z-component of vorticity ω_z/ω_0 on z = 0 plane at $t = 450t_A$, $500t_A$, and $550t_A$. White arrows represent the flow patterns. The vector scale is shown at the bottom of the left upper panel.

secondary-transportation of magnetic flux is maintained, ensuring that reconnection can proceed.

As shown in Fig. 5, if k_z of the most unstable modes retain their sign, k_y of these modes change sign at opposite side of the current sheet center. This implies that the tilting

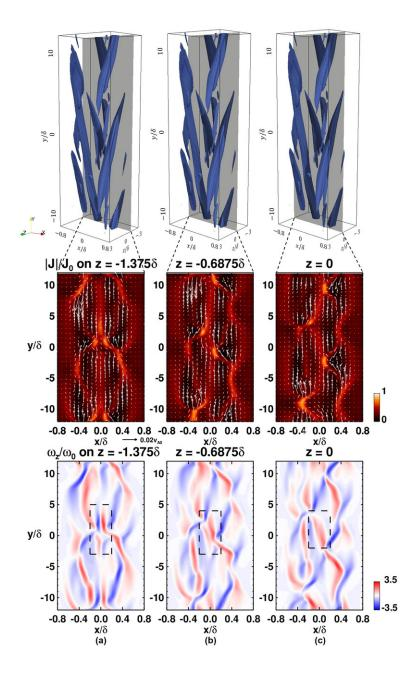


Fig. 11.— Upper panel: 3D surface of current density $|\mathbf{J}|/J_0 = 0.12$ in the simulation box. Black translucent surfaces are the planes at $z = -1.375\delta$, -0.6875δ , and 0 at $t = 500t_A$. Middle panel: Snapshots of $|\mathbf{J}|/J_0$ on the planes shown in the upper panel. White arrows represent the flow patterns. Lower panel: Corresponding ω_z/ω_0 contour plots.

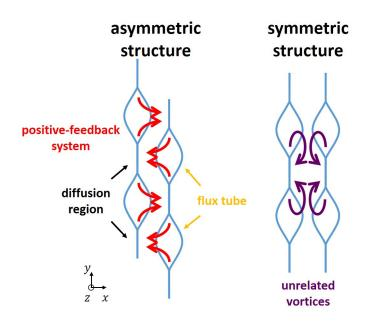


Fig. 12.— Cartoon of the layout of diffusion regions across the global current sheet. Red and purple arrows represent the characteristic flows on the xy-plane.

angles of the diffusion lines (defined as the angles between the orientations of the diffusion lines and the xz-plane) differ at either side of the global sheet, as shown in the flux tubes of Fig. 6. The tilting angle is defined as:

$$\theta = \arctan\left(\frac{\langle B_y \rangle_x}{\langle B_z \rangle_x}\right). \tag{13}$$

Therefore, the configuration of the diffusion regions changes in different xy-planes along z-axis. Fig. 11 plots the same variables as Fig. 10 but at different z-positions ($t = 500t_A$). Unlike their appearance in the z = 0 plane, the diffusion regions on the different tearing layers shift in the y-direction and sometimes show a symmetric structure (in which diffusion regions on different resonance layers align along the x-direction). In this configuration, the two diffusion regions do not cooperatively interact; thus no feedback character is established. The transition can be tracked by observing the pattern delineated by the dashed rectangle in the lower panel of Fig. 11. To an observer moving along the z-direction,

the diffusion regions form an alternating asymmetric-symmetric-asymmetric structure. A cartoon of these structures are presented in Fig. 12.

To examine the global structure of the positive-feedback system built by multiple tearing layers, we plot the 3D and 2D spatial distributions of the local v_x (see Fig. 13). Once the outflow region of a certain reconnection site couples with the inflow region of another site, the surface of relatively high v_x continuously extends across the current sheet center. Here, we select a cutoff surface of $v_x/v_{A0} = \pm 0.0005$, approximately 20% of the maximum absolute value of v_x/v_{A0} throughout the box. The dashed rectangles in panels (a) and (b) of Fig. 13 highlight where the surface crosses the black translucent plane (the central plane of the current sheet at x = 0). On this plane, the v_x contour plot exhibits an oblique checkered pattern, as it is presented in Fig. 13(d). The same features are highlighted in the same regions. Noted that v_x is not enhanced at the corners of the checkered pattern, because the diffusion regions are symmetrized at those points. Where the diffusion regions become asymmetric, the positive-feedback system establishes provided that a little shift occurs between the diffusion regions. Thus, the v_x is distinctly enhanced along the borders of the checks.

In summary, the diffusion regions in different resonance layers couple via their inflow and outflow regions. This configuration, the positive-feedback system, globally occurs inside the box, and underlies the rapid reconnection observed in our model.

3.4. Global inflow and slow-mode shocks

The enhanced reconnection rate in the basic model implies that a large amount of magnetic energy is transported into the current sheet. To evaluate the rate of energy transport, we investigate the global inflow along the x-boundary of the central current

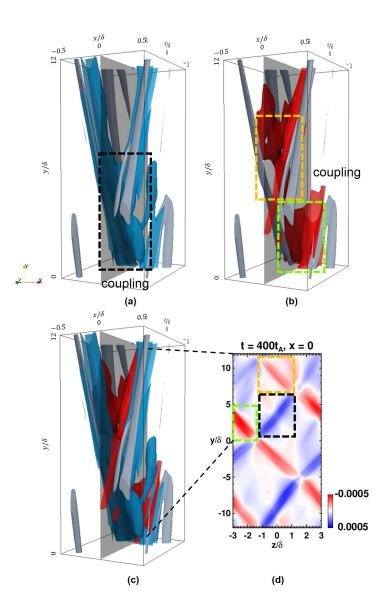


Fig. 13.— (a)-(c) Surface plots of v_x and $|\mathbf{J}|$ in the 3D box. Grey surface represents $|\mathbf{J}|/J_0 = 0.12$. Blue and red surfaces denote $v_x/v_{A0} = -0.0005$ and 0.0005 respectively. Black, green and yellow dashed rectangles highlight the coupling of inflow and outflow regions. (c) combines panels (a) and (b). (d) is the 2D contour plot of v_x on the translucent plane in (a)-(c). The same features are highlighted in the the same regions.

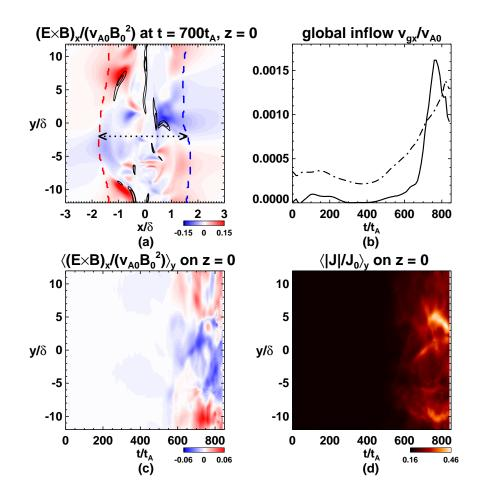


Fig. 14.— (a) Normalized Poynting flux at $700t_A$ on the z = 0 plane. Black contours indicate the enhanced current density $|\mathbf{J}|/J_0 \ge 0.8$. Current sheet boundary ($p_c = 0.008B_0^2$) is marked by the red and blue dashed lines to the left and right of x = 0, respectively. (b) Averaged global inflow (black solid line) and reconnection rate (black dash-dotted line). (c) and (d) Spatially averaged normalized $(\mathbf{E} \times \mathbf{B})_x$ and $|\mathbf{J}|$ inside the current sheet indicated by the dotted double arrows in (a).

sheet (Fig. 14). Fig. 14(a) exhibits snapshot of the normalized Poynting pattern $(\mathbf{E} \times \mathbf{B})_x$ at the time of Fig. 2(d) (namely, at $t = 700t_A$). The black contours indicate where the current density is locally enhanced. The surfaces assumed in the average inflow calculation are highlighted by the colored dashed lines to the left and right of the global current sheet.

They are the same surfaces used in the reconnection rate calculation. The average global inflow is determined as follows:

$$v_{gx} = \frac{\oint (\mathbf{E} \times \mathbf{B}) \cdot \mathbf{dS}}{2B_0^2 L_y L_z} \tag{14}$$

where **E** is the electric field and **dS** denotes the surface on global current sheet boundary. We consider the dot product to be only the x-component of $\mathbf{E} \times \mathbf{B}$, thus $|\mathbf{dS}| = dydz$. This quantity reflects the transport rate of the Poynting flux into the current sheet in the x-direction. As shown in Fig. 14(b), the v_{gx} changes smoothly over time. Panels (c) and (d) of Fig. 14 present time profiles of the normalized $\mathbf{E} \times \mathbf{B}$ and $|\mathbf{J}|$, respectively. Both variables are spatially averaged inside the current sheet as follows (where f denotes a variable)

$$\langle f \rangle_y = \frac{\int_{x_l(y)}^{x_r(y)} f(x, y, z = 0) dx}{x_r(y) - x_l(y)}.$$
(15)

In Eq. (15), $x_l(y)$ and $x_r(y)$ denote the positions of the left and right boundaries, respectively, of the current sheet at (y, z = y, 0). The diffusion region is asymmetric in the z = 0 plane at $t = 700t_A$, as observed in Fig. 14(a). Consequently, the inflow regions extending from the current sheet are also asymmetric. This pattern becomes increasingly obvious as local reconnection is accelerated by positive-feedback system (Fig. 14(c)). When entering the turbulent state (after $\sim t = 600t_A$; see Fig. 14(d)), the dense regions essentially overlap with the structures of Fig. 14(a) and (c), and the current density inside the current sheet is universally enhanced. Although the inflow structure is segmented, the global effect can be regarded as a single long diffusion region. Moreover, beyond $t = 400t_A$, the v_{gx} well correlates with the reconnection rate (black dash-dotted line in Fig. 14(b)). The enhanced v_{gx} suggests that, on macroscopic scale, magnetic energy is carried into the global current sheet by the flow and converted into other forms of energy. This suggestion is supported by the rising reconnection rate in later phase. The average global inflow exceeds the reconnection rate at approximately $t = 700t_A$, indicating that a small portion of the magnetic energy is stored before being gradually consumed.

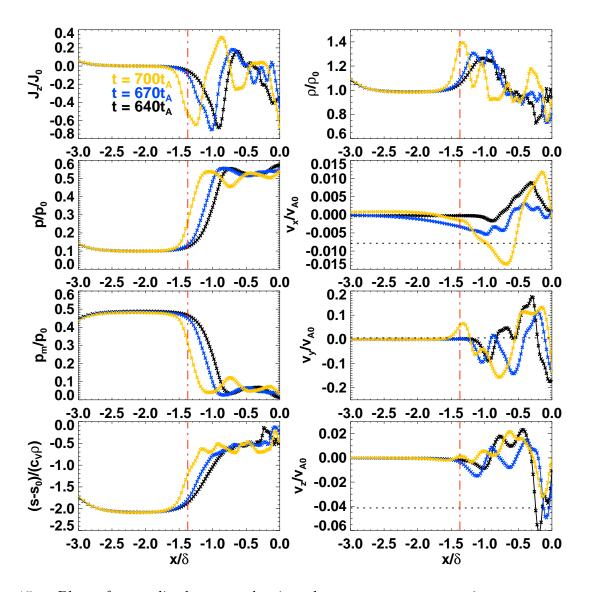


Fig. 15.— Plots of normalized current density, plasma pressure, magnetic pressure, entropy, plasma density and velocity across (y, z = 0, 0), showing the development of a slow-mode shock. Variables are plotted at $t = 640t_A$ (black solid lines), $670t_A$ (blue solid lines), $700t_A$ (orange solid lines). Crosses indicate the grid points. Red dash-dotted line is the detected shock front at $t = 700t_A$. Black horizontal dotted lines denote the shock speed in lab-frame.

When the inflow enhancement is high, slow-mode shocks gradually form between the inward flow and the outwardly growing flux tube. Along with reconnection in the diffusion region, these shocks are a likely mechanism of magnetic energy conversion. Shocks are identified by comparing the upstream and downstream quantities in the shock frames at selected points. Slow-mode shocks in the simulation domain are required to satisfy the following criteria:

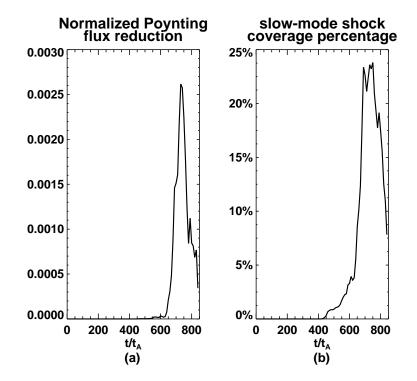
1. Rankine-Hugoniot relations: The Rankine-Hugoniot relations in the downstream must not deviate by more than 30% of their upstream values (Saito et al. 1995);

2. Velocities must satisfy $v_{Au} \ge v_{nu} \ge v_{slu}$, where v_{nu} is the normal component (perpendicular to the shock front) of the upstream velocity. v_{Au} and v_{slu} are the Alfvén speed and the slow-mode wave phase speed, respectively, in the upstream;

3. $v_{nd} \leq v_{sld}$, where v_{nd} denotes the normal component of the downstream flow speed and v_{sld} is the slow-mode wave phase speed in the downstream;

4. The **B** and **v** of the upstream and downstream must be co-planar (within 10°).

Fig. 15 shows the development of a slow-mode shock wave. Plotted are the current density J_z/J_0 , plasma pressure p/p_0 , magnetic pressure p_m/p_0 , entropy $(s - s_0)/c_V$, plasma density ρ/ρ_0 , plasma velocity v_x/v_{A0} , v_y/v_{A0} and v_z/v_{A0} across (y, z = 0, 0) in laboratory frame at three time points (for tracking the transition). The entropy is normalized by $s_0 = c_V \ln(p_0/\rho_0^{\gamma})$, where c_V is the specific heat at constant volume. The shock speed in the laboratory frame is indicated by the black dotted line in the plasma velocity plots. At $t = 640t_A$ (black solid lines in Fig. 15), the density is compressed around $x = -\delta$. The local J_z is minimized at the x-axial boundary of the flux tube. At this moment, the local x-directional flow on either side of the flux tube boundary is relatively weak. As the reconnection becomes more efficient, the flux tube thickens and expands in the negative x-direction. The relative flow between inside and outside of the tube boundary increases, further compressing the local plasma (compression occurs around $x = -1.3\delta$). Eventually (at $t = 700t_A$), the shock criteria are reached. The approximate position of the shock front is indicated line in Fig. 15. We fail to find the rotational discontinuity



previously reported in reconnection with a guide field (e.g., Longcope et al. 2009).

Fig. 16.— Temporal evolutions of (a) normalized energy conversion capability of shock M_s between the upstream and downstream of slow-mode shocks throughout the simulation box, and (b) percentage area coverage of slow-mode shock.

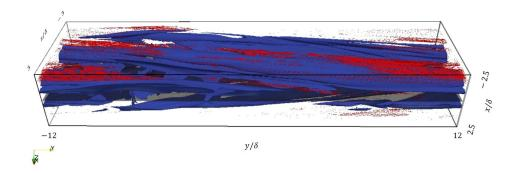


Fig. 17.— All detected shocks (indicated by red dots) are located approximately by downstream position at $t = 700t_A$. Blue surface represents $J_z = 0$.

Along with local Ohmic heating, these slow-mode shocks are considered as an additional source of magnetic energy consumption, as shown in Petschek's work. The energy conversion capability of shock (reduction of Poynting flux across the shock) M_s is calculated as:

$$M_s = \frac{\sum [(\mathbf{E} \times \mathbf{B})|_u - (\mathbf{E} \times \mathbf{B})|_d] \cdot dS}{2B_0^2 L_y L_z}.$$
(16)

The first and second terms of numerator denote the upstream and downstream Poynting vectors, respectively. The M_s is plotted as a function of time in Fig. 16(a). The efficiency of these shocks is greatly increased at the end of the simulation. To understand the global layout of the slow-mode shocks, we calculate the total percentage area coverage SC of the shock:

$$SC = \frac{S_{ss}}{4L_y L_z} \times 100\%$$
(17)

where S_{ss} is the total area covered by the shock. The coefficient "4" in the denominator indicates that four tearing layers coexist in the central current sheet. The temporal evolution of SC is plotted in Fig. 16(b). Both M_S and SC increase from $t = 450t_A$. Especially in the later phase, when the global inflow booms (after $t = 650t_A$), large extent of slow-mode shocks with efficient energy conversion capability are detected. The approximate downstream positions of all shocks found in the domain are highlighted in red in Fig. 17. The blue isosurface is the flux tube surface with $J_z = 0$.

In summary, multiple tearing layers construct a positive-feedback system that promotes reconnection. Large amount of magnetic energy is transported into the current sheet and converted to other forms of energy. Outwardly growing flux tubes collide with the strong inflow, gradually arousing slow-mode shocks along the tube boundaries. These shocks further enhance the reconnection. Therefore, we refer to our model as the "shock-evoking positive-feedback" model.

4. Discussion

In our present model, the reconnection rate is enhanced by non-linear interactions among multiple (tearing) layers. Our observed interactions resemble the double tearing mode (DTM) reported in the previous studies (e.g., Furth et al. 1973). Several comparisons are worth a brief mention here. First, the unperturbed state of DTM has multiple independent current sheets, whereas our model begins with a single current sheet. The multiple current layers are consequent to the growth of the tearing layers by mixed perturbations. Such growth of multiple layers requires a 3D system and a moderate guide field. Second, DTM is essentially a 2D process because translational invariance is assumed along the guide field direction (e.g., Janvier et al. 2011). Therefore, the arrangement of diffusion regions are maintained in that direction. In our model, the arrangement of diffusion regions differs among z-positions (see Section 3.3) and periodically changes from symmetric to asymmetric. Because of this non-uniformity, positive-feedback system is intermittently distributed. Our model is expected to consume magnetic energy less efficiently than DTM. Nevertheless, our model substantially enhances the reconnection rate. Third, as also shown in Section 3.3, the energy release may be slow in regions of symmetric arrangement of diffusion regions from different tearing layers. Notably, however, reconnection proceeds in symmetric DTM structures albeit very slowly (Yan et al. 1994). This result is consistent with our model.

In applying our model to realistic systems, such as solar flares, we must reconsider the boundary effects and the resistivity, which is much larger in our model than in solar phenomena. In our simulation, the selection of the tearing layers is highly influenced by the box size; in other words, by the aspect ratio of the initial current sheet. In a much larger system enclosing a current sheet with an extremely large aspect ratio, the evolution should be influenced by the boundary effects. If the plasma β is high in the current sheet, local Alfvén speed is slow. The evolution may be locally determined and the system will behave as an open system with free outflows. In low- β plasma, the evolution is globally determined and influenced by the boundary conditions at both ends of the field lines. Meanwhile, the most unstable tearing mode depends on both the resistivity and the guide field. However, we argue that once the emerging multiple tearing layers are sufficiently close to interact (separated within several $1/|\Delta'|$, where $1/|\Delta'|$ is the width of tearing layer), a positive-feedback system is built. Conversely, if the multiple layers approach very closely (within $1/|\Delta'|$), they will behave as a single layer. These propositions require investigation in further study; for instance, we should elucidate the scaling law that relates the Lundquist number to the reconnection rate, survey the guide field strength parameter and investigate the boundary condition. We must also improve the resolution and precision of our simulation.

Finally, we propose an extended model based on our "shock-evoking positive-feedback" model, which operates similar to 2D hierarchical reconnection. In the later phase of our simulation, long and thin current sheets with sheared magnetic structures remain near the center, which are candidate structures for further tearing. Daughton et al. (2011) simulated reconnection in a single current sheet under a guide field effect in the kinetic regime. They reported secondary flux ropes resulting from tearing instability. No secondary filamentary structure is observed in our model, likely because of the low resolution. Higher-ranking filaments are expected in our model when the Lundquist number and resolution are improved. Once the extended current sheet becomes unstable to the tearing instability, there are two possibilities. If the most unstable mode is centralized, a single tearing layer can be identified, as occurs in 2D plasmoid instability. Conversely, if the most unstable mode is oblique (Baalrud et al. 2012), multiple tearing layers should emerge. The coexisting multiple layers resemble the primary current sheet structure. Once established, the positive-feedback system enhances local reconnection. Flux tubes at the same side

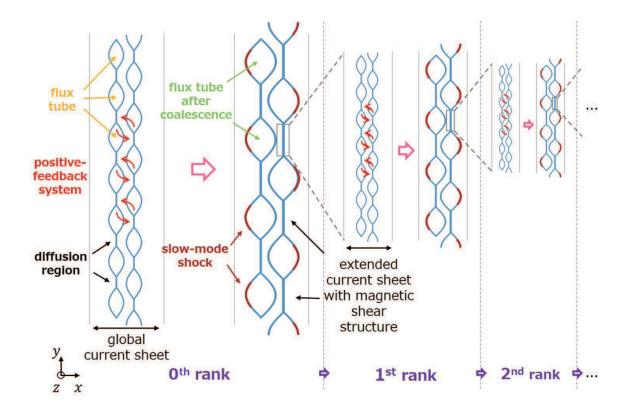


Fig. 18.— Illustration of hierarchical structure in the "shock-evoking positive-feedback" model.

grow and merge with each other. Slow-mode shocks are evoked along the outer boundary, while extended current sheets form between the coalesced flux tubes. These remaining current sheets might be subject to further tearing instability. Therefore, in a series of steps, the global structural scale of the diffusion region could reduce to microscopic size (such as the ion inertial scale) by alternate applications of 2D plasmoid instability and the 3D "shock-evoking positive-feedback" model. We regard this fractal structure of the current sheet generated by the "shock-evoking positive-feedback" model as an extension of the hierarchical structure of 2D plasmoid instability. Our scenario is illustrated in Fig. 18, assuming that multiple tearing layers are realized in each rank.

5. Summary

In this study, we simulate a 3D MHD magnetic reconnection across a symmetric current sheet with a finite guide field. We assume a uniform resistive environment and randomly perturb the initial velocity field. When relaxing the variation along the direction of the guide field, we find that the guide field increases the reconnection rate of the whole current sheet by several times, relative to the simulation with no guide field. Most unstable tearing modes, with components in the sheet-wise direction, emerge on multiple resonance layers. The diffusion regions on these layers establish a zigzag pattern that couple the inflow region and outflow region on different layers. Consequently, the outflow is diverted into the inflow region, ensuring that reconnection proceeds in the opposite layer. Gradually, the inflow from outside of the global current sheet also becomes accelerated by continuous activation of individual reconnection site. This enhanced inflow arouses slow-mode shocks along the outer boundary of the current sheet, further promoting energy conversion. We refer to our model as the "shock-evoking positive-feedback" model.

The Lundquist number is much smaller in our numerical experiment than in the solar corona. Therefore, our model is not directly applicable to real solar activities. To understand the feasibility of the "shock-evoking positive-feedback" in low resistive environments, we must conduct a parameter survey on the diffusivity magnitude. Altering the resistivity and guide field strength would induce different most unstable tearing modes, thus changing the topology of the positive-feedback system. In future study, we will further evaluate the effectiveness of our model by varying B_z and $\tilde{\eta}$.

The limited resolution of our model precludes the detection of finer filamentary structure. If the remaining long, thin current sheet becomes vulnerable to tearing instability, the internal sheared structure might develop into a higher-ranking positivefeedback system. The mechanism of the "shock-evoking positive-feedback" model would then enhance the local reconnection rate. In this way, the pattern could be repeated on ever smaller scales, eventually reaching the microscopic scale in environments of large Lundquist number. Therefore, we have potentially expanded 2D fractal reconnection into a 3D hierarchical structure with a high energy conversion rate. This capability of our model needs to be tested on very fine simulation grids, another goal of our future work.

This research was conducted using the Fujitsu PRIMEHPC FX10 System (Oakleaf-FX,Oakbridge) in the Information Technology Center, The University of Tokyo. Numerical computations were in part carried out on Cray XC30 at Center for Computational Astrophysics, National Astronomical Observatory of Japan. This research is supported by Leading Graduate Course for Frontiers of Mathematical Sciences and Physics (FMSP) and JSPS KAKENHI Grant Number 15H03640.

REFERENCES

- Baalrud, S. D., Bhattacharjee, A. and Huang, Y.-M. 2012, Physics of Plasmas, 19, 022101
- Bárta, M., Büchner, J., Karlický, M and Skála, J. 2011, ApJ, 737, 24
- Bellan, P. M. 2006, Fundamentals of Plasma Physics, Cambridge, UK
- Biskamp, D. 1986, Physics of Fluids, 29, 1520-1531
- Dahlburg, R. B., Antiochos, S. K. and Zang, T. A. 1992, Physics of Fluids B: Plasma Physics (1989-1993), 4, 3902-3914
- Dahlburg, R. B. and Einaudi, G. 2002, Physics Letters A, 294, 101-107
- Daughton, W., Roytershteyn, V., Karimabadi, H., Yin, L., Albright, B. J., Bergen, B. and Bowers, K. J. 2011, Nature Physics, 7, 539-542
- Furth, H. P., Killeen, J. and Rosenbluth, M. N. 1963, Physics of Fluids, 6, 459-484
- Furth, H. P., Rutherford, P. H. and Selberg, H. 1973, Physics of Fluids, 16, 1054-1063
- Galeev, A. A. and Zelenyi, L. M. 1977, ZhETF Pisma Redaktsiiu, 25, 407-411
- Janvier, M., Kishimoto, Y. and Li, J. Q. 2011, Physical Review Letters, 107, 195001
- Kudoh, T., Shibata, K. and Matsumoto, R. 1999, in Astrophysics and Space Science Library, Vol. 240, Numerical Astrophysics, ed. S. M. Miyama, K. Tomisaka and T. Hanawa, 203
- Landi, S., Londrillo, P., Velli, M. and Bettarini, L. 2008, Physics of Plasmas, 15, 012302
- Lapenta, G. 2008, Physical Review Letters, 100, 235001
- Lapidus, A. 1967, Journal of Computational Physics, 2, 154-177

Longcope, D. W., Guidoni, S. E. and Linton, M. G. 2009, ApJ, 690, L18-L22

- Loureiro, N. F., Samtaney, R., Schekochihin, A. A. and Uzdensky, D. A. 2012, Physics of Plasmas, 19, 042303
- Onofri, M., Primavera, L., Malara, F. and Veltri, P. 2004, Physics of Plasmas, 11, 4837-4846
- Parker, E. N. 1963, ApJS, vol. 8, 177
- Petschek, H. E. 1964, NASA Special Publication, 50, 425
- Saito, Y., Mukai, T., Terasawa, T., Nishida, A., Machida, S., Hirahara, M., Maezawa, K., Kokubun, S. and Yamamoto, T. 1995, Journal of Geophysical Research, Vol. 100, No. A12, 23567-23582
- Shibata, K. and Tanuma, S. 2001, Earth, Planets, and Space, 53, 473-482
- Sweet, P. A. 1958, Electromagnetic Phenomena in Cosmical Physics, 6, 123
- Yan, M., Otto, A., Muzzell, D. and Lee, L. C. 1994, Journal of Geophysical Research, Vol. 99, No. A5, 8657-8669

This manuscript was prepared with the AAS IATEX macros v5.2.